

# Quantum dot energy levels in bilayer graphene: Exact and approximate study

G. Giavaras

*Instituto de Ciencia de Materiales de Madrid (ICMM),  
Consejo Superior de Investigaciones Científicas (CSIC), Sor Juana Inés de la Cruz 3, 28049 Madrid, Spain*

In bilayer graphene the exact energy levels of quantum dots can be derived from the four-component continuum Hamiltonian. Here, we study the quantum dot energy levels with approximate equations and compare them with the exact levels. The starting point of our approach is the four-component continuum model and the quantum dot is defined by a continuous potential well in a uniform magnetic field. Using some simple arguments we demonstrate realistic regimes where approximate quantum dot equations can be derived. Interestingly these approximate equations can be solved semi-analytically, in the same context as a single-component Schrödinger equation. The approximate equations provide valuable insight into the physics with minimal numerical effort compared with the four-component quantum dot model. We show that the approximate quantum dot energy levels agree very well with the exact levels in a broad range of parameters and find realistic regimes where the relative error is vanishingly small.

## I. INTRODUCTION

The versatile electronic properties of bilayer graphene (BLG) [1, 2], along with experimental advancements have enabled the fabrication of highly controllable quantum devices which might find applications in emerging quantum technologies. Quantum dots (QDs) are among these quantum devices and various studies have explored control and manipulation of confined charge, valley, and spin states [3–15]. In BLG confined quantum states can be defined by electrostatic gates providing a simple and attractive platform to realize tunable quantum dots [14, 15]. A perpendicular magnetic field can lift the valley degeneracy offering additional control of the discrete energy levels and quantum states of the QD. The resulting QD can be used to host qubits [8, 9] which can be efficiently controlled with external electric and magnetic fields. Beyond the spectroscopic investigation and characterization of single QDs in BLG [12], coherent charge oscillations have been successfully demonstrated [16] and measurements of valley [7] and spin lifetimes [3] have been performed.

From a theoretical point of view, many theoretical works on QDs in BLG focus on hard-wall potential wells because the resulting QD equations are drastically simplified and can be studied semi-analytically [8, 9, 11]. However, hard-wall potentials are usually not realistic enough and therefore fail to capture the complete physics. In addition, the majority of theoretical works uses solely numerical routines to study the energy levels of the QDs, without providing any essential pedagogical insight into the underlying physics. This occurs despite the fact that many interesting physical regimes in a bilayer QD system can be treated approximately and with high accuracy. Approximate methods are therefore a necessary and powerful tool [17, 18] to better understand the properties of QDs in BLG.

In the present work we start with the four-component continuum model and define the QD with a continuous potential well in a uniform magnetic field. We explore potential wells with soft-wall and hard-wall profiles and demonstrate that it is possible to derive approximate single-component equations to calculate the energy levels of the QD in a broad range of parameters. The main advantage is that the approximate equa-

tions can be solved semi-analytically in the same context as a single-component Schrödinger equation. We can thus obtain valuable insight into the physics and predict the correct features of the QD energy levels at different magnetic fields and potential well profiles. We show that the approximate QD levels are in a very good agreement with the exact QD levels derived from the four-component continuum model. Interestingly, in some realistic QD regimes the induced errors are vanishingly small indicating that the approximate equations are reliable and capture all the important physics.

We describe in Sec. II the physical model of the QD in BLG based on the four-component continuum model. We continue in Sec. III to detail the necessary steps that allow us to derive the approximate QD equations. In Sec. IV we identify with specific examples some QD regimes that can be studied approximately. In Sec. V a detailed comparison is made between the exact and the approximate QD energies demonstrating the accuracy of our method. The conclusions of the work are summarized in Sec. VI, and some further results are presented in Appendix A.

## II. PHYSICAL MODEL

In this section we describe the quantum dot formed in a bilayer graphene lattice with Bernal stacking [1]. In the four-component continuum model the envelope functions describing the QD system in the vicinity of the  $K$  valley can be written in the form:  $\Psi = (\psi_A, \psi_B, \psi_{B'}, \psi_{A'})^T$ , where the subscripts  $A, B$  and  $A', B'$  denote the corresponding sublattices in the upper and lower graphene layers respectively. When trigonal warping effects are ignored the QD can be accurately described by the Hamiltonian

$$H_{\text{QD}} = \begin{pmatrix} V_1 & u_0\pi & t_c & 0 \\ u_0\pi^\dagger & V_1 & 0 & 0 \\ t_c & 0 & V_2 & u_0\pi^\dagger \\ 0 & 0 & u_0\pi & V_2 \end{pmatrix}, \quad (1)$$

with  $\pi = (p_x + ip_y)$ ,  $\pi^\dagger = (p_x - ip_y)$ , and  $(p_x, p_y) = \mathbf{p}$  being the 2D momentum operator. We consider an external

magnetic field  $B$  perpendicular to the BLG ( $z$ -direction) described by the vector potential  $\mathbf{A}$ . For a cylindrically symmetric system the vector potential is nonzero in the azimuthal  $\theta$ -direction,  $\mathbf{A} = (0, A(r), 0)$ , with  $A(r) = Br/2$  and the operator  $\mathbf{p}$  is replaced by  $\mathbf{p} + e\mathbf{A}$  when  $B \neq 0$ . The parameter  $t_c$  is a constant interlayer coupling which is taken to be  $t_c = 400$  meV together with the lattice parameter  $u_0 = 10^6$  m s $^{-1}$ .

We also add to the bilayer system an electrostatic potential term,  $V_{\text{QD}}(r)$ , that models the QD potential well, and specifically we consider that

$$V_{1,2}(r) = V_{\text{QD}}(r) \pm \tau \frac{V_b(r)}{2}, \quad (2)$$

where  $V_b$  denotes a bias between the two graphene layers. In a QD system  $V_b$  is usually assumed to be constant, however, the approximate method developed in Sec. III is general enough and can be applied to QDs with a position dependent bias. We assume a gate-induced QD and model the QD potential well as

$$V_{\text{QD}}(r) = \frac{-V_W}{\cosh(r/L_W)^s}. \quad (3)$$

The exact profile of the QD potential is determined by the parameters  $V_W$ ,  $L_W$ ,  $s$ . We consider a few values of  $s$  in order to simulate either a smooth potential well (soft-wall) which arises for smaller  $s$  values, or a much steeper potential well (hard-wall) with a relatively flat bottom. In Eq. (2) we take  $\tau = 1$  for the  $K$  valley and also consider  $\tau = -1$  for the  $K'$  valley. Note, however, for  $K'$  the two graphene layers in the envelope functions are exchanged.

Because both  $A$  and  $V_{\text{QD}}$  depend on the radial only coordinate the resulting eigenvalue problem describing the QD,  $H_{\text{QD}}\Psi(r, \theta) = E\Psi(r, \theta)$ , can be simplified by eliminating the  $\theta$  dependence. This is achieved with the substitution

$$\Psi(r, \theta) = \frac{1}{\sqrt{r}} \begin{pmatrix} \phi_A(r)e^{im\theta} \\ i\phi_B(r)e^{i(m-1)\theta} \\ \phi_{B'}(r)e^{im\theta} \\ i\phi_{A'}(r)e^{i(m+1)\theta} \end{pmatrix}, \quad (4)$$

which leads to the following coupled equations for the radial components of the QD states

$$\left(\gamma \frac{d}{dr} + L_1\right) \phi_B + t_c \phi_{B'} = (E - V_1) \phi_A, \quad (5a)$$

$$\left(-\gamma \frac{d}{dr} + L_1\right) \phi_A = (E - V_1) \phi_B, \quad (5b)$$

$$\left(\gamma \frac{d}{dr} + L_2\right) \phi_{A'} + t_c \phi_A = (E - V_2) \phi_{B'}, \quad (5c)$$

$$\left(-\gamma \frac{d}{dr} + L_2\right) \phi_{B'} = (E - V_2) \phi_{A'}, \quad (5d)$$

with the parameter  $\gamma = u_0 \hbar$  and the terms

$$L_{1,2}(r) = \mp \gamma \frac{m \mp \frac{1}{2}}{r} \mp \gamma \frac{e}{\hbar} A(r), \quad (6)$$

which account for the angular momentum, denoted by the integer  $m$ , and the magnetic vector potential in the azimuthal direction.

### III. DERIVATION OF APPROXIMATE QUANTUM DOT EQUATIONS

In this section we outline the basic steps that allow us to simplify the four-component continuum model of the QD and derive an approximate single-component equation. This equation gives the QD energies of the confined states. Alternatively, we could use as a starting point the well known two-component continuum model and perform further simplifications in order to obtain an approximate equation. In this approach, however, the approximate energies can be computed only within the range of validity of the two-component model. For this reason, this approach is expected to be less accurate and for clarity of presentation we start directly with the four-component model.

Analytical calculations in the Landau regime [19] have shown that the two components  $\phi_A$  and  $\phi_{B'}$  can be expressed with the same analytical functions and the difference  $|\phi_A| - |\phi_{B'}|$  becomes smaller as  $m$  increases. Based on these observations the first step in our method is to eliminate the two components  $\phi_B$  and  $\phi_{A'}$  and derive the coupled equations for the components  $\phi_A$  and  $\phi_{B'}$ . We use Eqs. (5a) and (5b) to eliminate  $\phi_B$ , and Eqs. (5c) and (5d) to eliminate  $\phi_{A'}$ . A simple analysis leads to

$$\left(\frac{d^2}{dr^2} + a_1 \frac{d}{dr} + b_1\right) \phi_A = \frac{t_c}{\gamma^2} (E - V_1) \phi_{B'}, \quad (7a)$$

$$\left(\frac{d^2}{dr^2} + a_2 \frac{d}{dr} + b_2\right) \phi_{B'} = \frac{t_c}{\gamma^2} (E - V_2) \phi_A, \quad (7b)$$

with the coefficients

$$a_j(r) = \frac{V_j'}{E - V_j}, \quad (8a)$$

$$b_j(r) = \frac{L_j}{\gamma} \frac{V_j'}{E - V_j} + \frac{L_j'}{\gamma} - \frac{L_j^2}{\gamma^2} + \frac{(E - V_j)^2}{\gamma^2}, \quad (8b)$$

$j = 1, 2$  and prime denotes the first derivative with respect to  $r$ . We then perform the transformation

$$\begin{pmatrix} \phi_A \\ \phi_{B'} \end{pmatrix} = \begin{pmatrix} (E - V_1)^{1/2} & 0 \\ 0 & (E - V_2)^{1/2} \end{pmatrix} \begin{pmatrix} w \\ \nu \end{pmatrix}, \quad (9)$$

and derive the two coupled equations for the functions  $w$  and  $\nu$

$$\left(\frac{d^2}{dr^2} + q_1\right) w = \frac{t_c}{\gamma^2} [(E - V_1)(E - V_2)]^{1/2} \nu, \quad (10a)$$

$$\left(\frac{d^2}{dr^2} + q_2\right) \nu = \frac{t_c}{\gamma^2} [(E - V_1)(E - V_2)]^{1/2} w, \quad (10b)$$

with

$$q_j(r) = b_j - \frac{1}{2} \frac{V_j''}{(E - V_j)} - \frac{3}{4} \left(\frac{V_j'}{E - V_j}\right)^2, \quad (11)$$

Equations (10a) and (10b) are exact, and to proceed with some approximations we set

$$\frac{1}{\lambda} = \frac{\nu}{w}, \quad (12)$$

and assume the function  $\lambda$  to be approximately constant in the region where the QD states are confined. This regime has been shown to be valid for the Landau states [19] but we expect deviations from this regime when  $V_W \neq 0$ , since the resulting confining region of the QD states is now modified. However, these deviations are small when the character (profile) of the Landau states is not significantly altered due to  $V_W$  [18], therefore  $\lambda$  can be assumed to be approximately constant beyond the Landau regime. This case has been demonstrated for different potential wells defining QDs in monolayer graphene [18, 20]; consequently, a similar framework should be valid in bilayer graphene. A characteristic example of small deviations from the Landau regime due to  $V_W \neq 0$  involves the creation of an extra node in the induced states [21]. This node lies in a region where the amplitude of the states is exponentially small, and as a result the creation of the node only weakly affects the character of the Landau states [21].

Substituting Eq. (12) into Eqs. (10a) and (10b) and neglecting terms containing derivatives of  $\lambda$  we derive from Eq. (10a) that

$$\frac{1}{\lambda} = \frac{\gamma^2}{t_c \sqrt{\kappa}} \left( \frac{1}{\nu} \frac{d^2 \nu}{dr^2} + q_1 \right), \quad (13)$$

and simultaneously Eq. (10b) gives

$$\lambda = \frac{\gamma^2}{t_c \sqrt{\kappa}} \left( \frac{1}{\nu} \frac{d^2 \nu}{dr^2} + q_2 \right). \quad (14)$$

with  $\kappa = (E - V_1)(E - V_2)$ . Combining Eqs. (13) and (14) we derive that

$$\left( \frac{1}{\nu} \frac{d^2 \nu}{dr^2} + q_1 \right) \left( \frac{1}{\nu} \frac{d^2 \nu}{dr^2} + q_2 \right) - \frac{t_c^2}{\gamma^4} \kappa = 0 \quad (15)$$

which can be written in the compact form as

$$f^2 + (q_2 - q_1)f - \frac{t_c^2}{\gamma^4} \kappa = 0, \quad (16)$$

with the function  $f$  being

$$f = \frac{1}{\nu} \frac{d^2 \nu}{dr^2} + q_1. \quad (17)$$

This function contains all the QD parameters including the energy that we need to compute. One possible way to proceed is to write  $f$  in the form

$$f = \frac{1}{2}(q_1 - q_2) \pm \sqrt{\left( \frac{q_1 - q_2}{2} \right)^2 + \frac{t_c^2}{\gamma^4} \kappa}, \quad (18)$$

which is a formal solution to Eq. (16). The last two equations indicate that  $\nu$  should satisfy the second-order differential equation:

$$\frac{d^2 \nu}{dr^2} + Q_{\pm} \nu = 0, \quad (19)$$

with the coefficient

$$Q_{\pm}(r) = \frac{1}{2}(q_1 + q_2) \pm \sqrt{\left( \frac{q_1 - q_2}{2} \right)^2 + \frac{t_c^2}{\gamma^4} \kappa}. \quad (20)$$

In Sec. V we use Eq. (19) to derive the approximate energies of the QD. We usually need to consider only  $Q_+$ , since  $Q_- < 0$  everywhere along  $r$ . But, whether we have to account for  $Q_-$  depends on the exact parameters defining the QD as well as the energy range of interest.

Equation (20) can be slightly simplified in the limit where  $q_1 \approx q_2$ . The validity of this limit can be demonstrated by starting with Eqs. (10a) and (10b) and performing the transformation

$$\begin{pmatrix} w \\ \nu \end{pmatrix} = \frac{1}{2} \begin{pmatrix} 1 & 1 \\ 1 & -1 \end{pmatrix} \begin{pmatrix} \chi_+ \\ \chi_- \end{pmatrix}, \quad (21)$$

which leads to the following coupled equations

$$\left( \frac{d^2}{dr^2} + \tilde{Q}_- \right) \chi_+ = \frac{1}{2}(q_2 - q_1) \chi_-, \quad (22a)$$

$$\left( \frac{d^2}{dr^2} + \tilde{Q}_+ \right) \chi_- = \frac{1}{2}(q_2 - q_1) \chi_+, \quad (22b)$$

with

$$\tilde{Q}_{\pm}(r) = \frac{1}{2}(q_2 + q_1) \pm \frac{t_c}{\gamma^2} [(E - V_1)(E - V_2)]^{1/2}. \quad (23)$$

Equations (22a) and (22b) are exact and suggest that  $q_2 \approx q_1$  when  $\chi_+ = w + \nu \approx 0$ , so that both sides of Eq. (22a) simultaneously vanish. As a result, with  $\chi_- = 2\nu$  the derived approximate equation for  $\nu$  becomes a second order equation identical to Eq. (19), but with  $Q_+$  replaced by  $\tilde{Q}_+$ . Our calculations show that  $Q_+$  gives more accurate approximate results and for this reason we use  $Q_+$  throughout this work.

We can numerically solve Eq. (19) to find the approximate  $E$  and  $\nu$ . However, using general arguments pertinent to confined quantum states [22], which have been found to be applicable to monolayer graphene [17, 18], we can make some further approximations. Specifically, considering that  $Q_+$  determines a physically acceptable state  $\nu$ , we can define the region of localisation from the condition  $Q_+ > 0$ . The simplest regime occurs at  $V_b = 0$  and when the singular point in  $q_1$  and  $q_2$ , satisfying  $E - V_{\text{QD}} = 0$ , can be safely ignored. We focus on a QD parameter range where  $Q_+$  has a single maximum away from  $r = 0$  and retain terms up to  $r^2$ . We then expand  $Q_+$  about  $r_0$

$$Q_+(r) \approx Q_+(r_0) + \frac{1}{2} Q_+''(r_0) (r - r_0)^2, \quad (24)$$

where  $r_0$  is the position of the maximum and  $Q_+''(r_0)$  is the second derivative of  $Q_+(r)$  at  $r_0$ , with  $Q_+''(r_0) < 0$ . An important observation is that  $r_0$  is generally energy dependent,  $r_0 = r_0(E)$ , and sensitive to the QD parameters. Equations (19) and (24) indicate that  $\nu$  obeys a single-component Schrödinger equation similar to that of a one-dimensional harmonic-oscillator located at  $r_0$ . Thus, the energy  $E$  of a physically acceptable confined state  $\nu$  should satisfy

$$\frac{Q_+(r_0)}{\sqrt{\frac{1}{2}|Q_+''(r_0)|}} = 2n + 1, \quad n = 0, 1, \dots \quad (25)$$

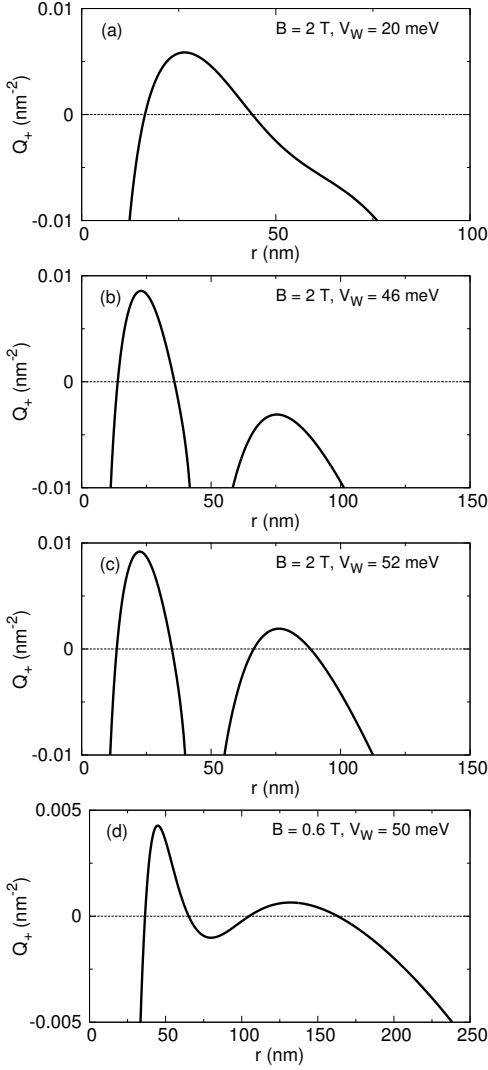


FIG. 1. The function  $Q_+$ , defined in Eq. (20), as a function of radial coordinate at different magnetic fields and potential wells for  $s = 2$ ,  $V_b = 0$ , and: (a)  $m = 2$ ,  $E \approx 1$  meV, (b)  $m = 2$ ,  $E \approx -20$  meV, (c)  $m = 2$ ,  $E \approx -25$  meV, and (d)  $m = 8$ ,  $E \approx 15$  meV.

where the integer  $n$  is the number of nodes of the state  $\nu$ . Equation (25) can be solved numerically, e.g., with bisection, to find the energy  $E$  for the corresponding value of  $n$ . Compared with the four-component continuum model Eq. (25) provides an approximate but much simpler way to extract the QD energy levels and explore how these QD levels emerge from the bulk Landau levels. The nodeless quantum state  $\nu$  has the exponential dependence

$$\nu(r) = e^{-(r-r_0)^2/2\sqrt{|Q'_+(r_0)|/2}}, \quad (26)$$

while “excited” states can be written in terms of Hermite polynomials [22]. The number of nodes of a QD state in monolayer graphene is sensitive to the position of the QD level relative to the potential well [21]. It is straightforward to show that this relativistic effect occurs also in a bilayer graphene QD but is not captured by the approximate Eq. (25). Consequently, within our approximate model a QD state, when

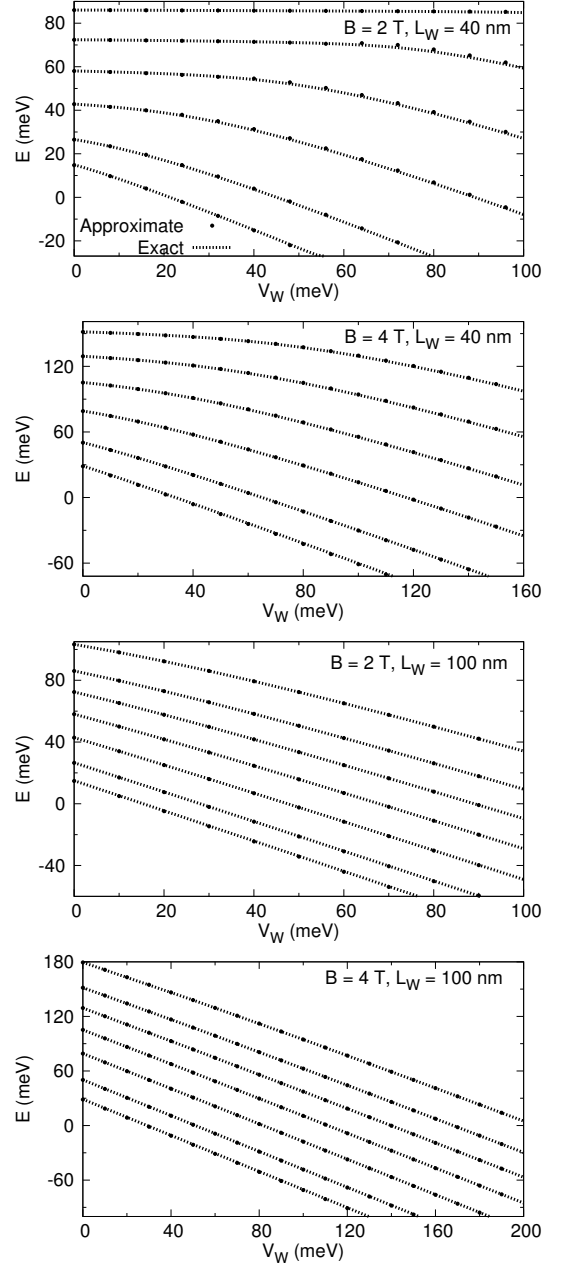


FIG. 2. Exact and approximate QD energy levels as a function of QD potential well for  $s = 2$ , and  $V_b = 0$ . From lower to upper curve:  $m = 2, 4, 7, 10, 13, 16, 20$ . Approximate QD levels are derived from Eq. (25) for  $n = 0$ .

$V_{\text{QD}} \neq 0$ , has the same number of nodes as the original Landau state. We further address this point in Sec. V.

#### IV. APPROXIMATE QUANTUM DOT REGIMES

In this section we describe the behavior of the function  $Q_+$  [Eq. (20)] that can arise in a QD, and specify the approximate QD regimes. Because  $Q_+$  can acquire a complicated spatial dependence that sensitively depends on the QD parameters,

as well as the exact QD energy range, it is useful to identify regimes with specific realistic examples.

In the simplest regime demonstrated in Fig. 1(a) the function  $Q_+$  has a single positive maximum. Here,  $Q_+$  arises for a QD energy which at  $V_W = 0$  corresponds to a positive bulk Landau level, and in this “single-maximum” regime the approximate energy can be derived from Eq. (25). In Fig. 1(a) we consider  $V_b = 0$  and adjust the QD parameters to give a QD energy greater than  $V_{\text{asym}}$ , with  $V_{\text{asym}} = V_{\text{QD}}(r \rightarrow \infty) \approx 0$ . It can be readily shown that by gradually increasing  $V_W$  the QD energy decreases and crosses  $V_{\text{asym}}$ , eventually resulting in a well-defined negative maximum in  $Q_+$  [see Fig. 1(b)]. A key observation is that the profile of the function  $Q_+$  continues to change at even larger values of  $V_W$  when the QD energy forms anticrossing points with energies that originally correspond to negative Landau levels (hole levels). This QD configuration, characterized by anticrossings for  $E < V_{\text{asym}}$ , has been demonstrated in monolayer graphene [20, 23] and to obtain the corresponding approximate QD energies a different method is needed from the one employed here.

Figure 1(c) presents  $Q_+$  for a typical case where anticrossing points can be observed in the QD energy spectrum for energies  $E < V_{\text{asym}}$  (Appendix A). Assuming  $V_b = 0$  the function  $Q_+$  has now two positive maxima separated by a central region where the singular point at  $r \approx 44$  nm dominates. According to the above remarks the approximate method developed in Sec. III becomes less accurate as  $V_W$  increases and the QD levels start to form anticrossings. The transition from the regime shown in Fig. 1(a) to that in Fig. 1(c) can be observed, for example, by increasing  $V_W$ . Between the two regimes Eq. (25) may still be used, provided the inner maximum of  $Q_+$  dominates. This implies that the QD state has negligible amplitude around the outer maximum, hence, this configuration is more likely to occur for small values of  $V_W$  (Sec. V).

Figure 1(d) shows another QD regime that arises when  $Q_+$  has again two positive maxima. The important, however, difference from the example in Fig. 1(c) is that now there is no singular point, i.e., the QD energy is greater than  $V_{\text{asym}}$ . In the regime shown in Fig. 1(d) the approximate QD energy is obtained from the numerical solution of Eq. (19), and as demonstrated in Sec. V the corresponding QD energy levels anticross for energies  $E > V_{\text{asym}}$ . Despite the simplicity of the approximate model the anticrossing points can be accurately predicted by Eq. (19). We emphasize that anticrossings are very common in the energy spectra of graphene QDs [20, 23], and in the present work we demonstrate how the position and the size of these anticrossings can be directly inferred from a simple inspection of the function  $Q_+$ .

Another approximate regime occurs for small  $m$  values and when  $B$  as well as  $L_W$  are large, so that the magnetic length  $l_B = (\hbar/eB)^{1/2}$  to be smaller than the effective width of the potential well. In this regime the state is localised near the center of the QD,  $r \approx 0$ , and to a good approximation the QD energy  $E$  decreases linearly with  $V_W$ . This can be understood from the fact that in the region where the state is localised the potential well induced terms in Eq. (20) containing derivatives of  $V_1$  and  $V_2$  are negligible. Therefore, to a

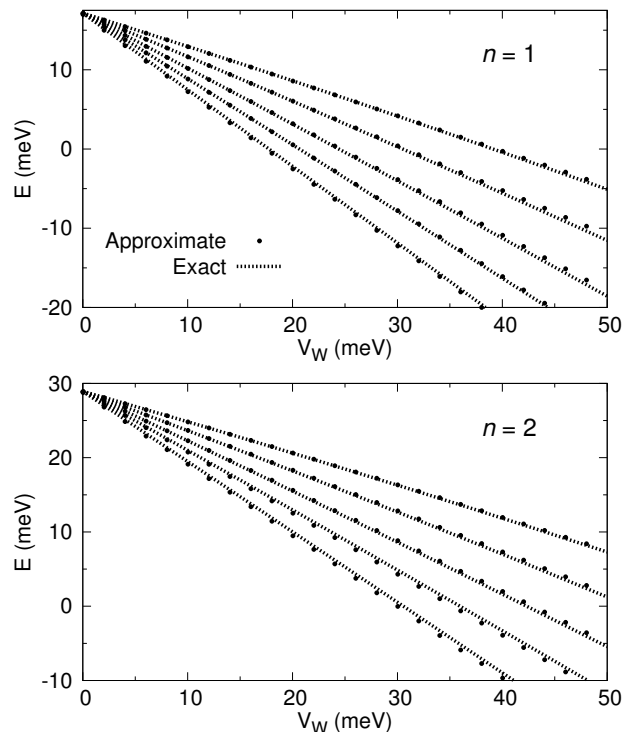


FIG. 3. Exact and approximate QD energy levels as a function of QD potential well for  $L_W = 100$  nm,  $B = 4$  T,  $s = 2$ , and  $V_b = 0$ . From lower to upper curve:  $m = -4, -16, -25, -35, -45$ . Approximate QD levels are derived from Eq. (25) for different  $n$  values.

good approximation  $V_{\text{QD}} \approx -V_W$ , within the region where the state is localised. Focusing on a positive Landau level  $E_L$ , and taking  $E = E_L$  at  $V_W = 0$  then by increasing  $V_W$  we eventually expect the energy  $E$  to cross  $V_{\text{asym}} \approx 0$ . A simple way to determine the linear dependence of  $E$  versus  $V_W$  is to use Eq. (25) to find the approximate  $V_W$  for which  $E \approx V_{\text{asym}}$ . By denoting this particular value of  $V_W$  by  $V_W^0$ , the approximate energy as a function of  $V_W$  can be written as

$$E(V_W) \approx E_L - E_L \frac{V_W}{V_W^0}. \quad (27)$$

In this approximate treatment the maximum value of  $V_W^0$  is  $E_L$ , therefore the linear drop cannot be greater than  $V_W$  as explicitly quantified in Sec. V with various numerical examples. This conclusion can be derived from a simple inspection of Eq. (25). Specifically, if Eq. (25) is satisfied for an energy  $E$  corresponding to a Landau level,  $E = E_L > 0$  at  $V_W = 0$  (Landau regime), then  $E = 0$  at  $V_W = E_L = V_W^0$  can also be a solution. At a fixed angular momentum and magnetic field the limit  $V_W^0 \approx E_L$  can be achieved by increasing the effective width  $L_W$  of the QD.

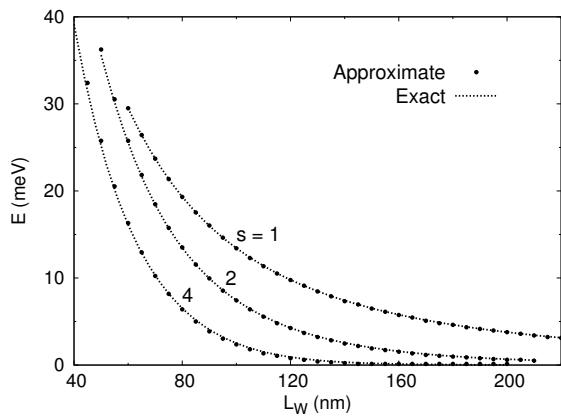


FIG. 4. Exact and approximate QD energy levels as a function of QD potential width for  $V_W \approx 48$  meV,  $m = 8$ ,  $B = 2$  T and different superscripts  $s$  in Eq. (3). Approximate QD levels are derived from Eq. (25) for  $n = 0$ . For clarity the curves for  $s = 1$  and  $s = 2$  are shifted by 20 nm and 10 nm respectively along the horizontal axis.

## V. COMPARISON BETWEEN EXACT AND APPROXIMATE ENERGIES

In this section we quantify the approximations made in Sec. III and compare the exact QD energy levels with the approximate ones. The exact levels are derived from the numerical solution of the four-component continuum QD model, Eqs. (5a)–(5d). The approximate levels are derived from the single component approximate Eq. (19). This is done either numerically, by solving Eq. (19), or applying directly the harmonic oscillator formula, Eq. (25).

For the numerical calculations of the exact QD levels we employ a similar numerical approach to that in Ref. 23. Some simple modifications are needed to apply the appropriate boundary conditions that result in a Hermitian eigenvalue problem [23]. In the present work the derivatives in the radial Eqs. (5a)–(5d) are approximated by a second-order finite-difference scheme with a discretization length  $\delta$ . Compared with the first-order scheme employed in Ref. 23 the advantage is that the numerical errors are of the order of  $\delta^2$ . The disadvantage is that the resulting matrix is less sparse, however, it can be easily treated using ARPACK subroutines incorporated into a python program. For the numerical calculations we take  $\delta < 0.2$  nm which ensures that the induced numerical errors are small and do not affect the comparison between the exact and the approximate QD levels.

The Landau regime ( $V_W = 0$ ) is the simplest regime to confirm that Eq. (25) can be used to obtain approximate energies for confined states. It can be easily verified by the analytical form of the Landau states [19] that  $w \approx \lambda\nu$  for  $t_c = 400$  meV. Additionally, the function  $Q_+$  defined in Eq. (20) for  $m \neq 0$  has a single positive maximum at  $r_0$ , and interestingly,  $r_0$  is now energy independent. This remark allows us to drastically simplify Eq. (25) and perform analytical calculations to derive the Landau levels. However, since the Landau levels have been analytically explored in detail in an earlier work [19] we do not pursue here a further investigation, and focus on the

QD regime corresponding to  $V_W \neq 0$ .

Figure 2 shows some QD energy levels as a function of the QD potential well  $V_W$ . The approximate levels have the correct dependence on  $V_W$  and agree very well with the exact levels in a broad range of  $V_W$  and different angular momenta  $m$ . At  $V_W = 0$  the approximate method reproduces the bulk Landau levels very accurately. When  $V_W \neq 0$ , then in general larger  $m$  levels are affected less by the potential well, and for a fixed  $m$  the role of  $V_W$  is more significant at larger magnetic fields [18, 20]. Furthermore, in agreement with the remarks in Sec. III, Fig. 2 demonstrates that at larger magnetic fields the QD levels exhibit an approximate linear dependence on  $V_W$ , which is more pronounced for smaller  $m$  values.

In Fig. 2, focusing on a given energy and gradually increasing  $V_W$  shifts this energy within the potential well,  $E < V_{\text{asym}} \approx 0$ . According to the exact QD model, Eqs. (5a)–(5d), when such a shift takes place extra nodes appear in the QD states as happens in monolayer graphene [21]. The key observation is that when  $V_W$  is not too large a node appears within a spatial region where the QD state has low amplitude [21]. Therefore, the formation of the extra node is not expected to alter significantly the physics. For this reason the approximate harmonic oscillator formula, Eq. (25), is still applicable and predicts the corresponding energy very accurately.

In Fig. 2 we only plot QD levels which emerge from positive bulk Landau levels, however, the approximate method can also be successfully applied to QD levels that originate from negative Landau levels (Appendix A). Similar to monolayer graphene [20], by increasing  $V_W$  some QD energy levels start to anticross for energies  $E < V_{\text{asym}}$ . The resulting QD levels arise from the hybridization between electron and hole Landau levels, and in this regime the function  $Q_+$  has the characteristic form shown in Fig. 1(c). As discussed in Sec. III this regime is beyond the scope of the present work and cannot be captured by Eq. (25).

Figure 3 presents some QD energy levels as a function of the QD potential well for negative  $m$  values. The agreement between the approximate energy levels and the exact ones is again very good especially for small values of  $V_W$ . Quantum dot levels can also emerge from the zero-energy Landau level, however, for these levels the assumption,  $1/\lambda = \nu/w$ , [Eq. (12)] is not satisfied and Eq. (25) cannot be applied. In this QD regime the singular point is expected to be important and a different strategy is needed to obtain the approximate QD energies. However, we can still obtain some physical insight without significantly deviating from the analysis in Sec. III. We can loosely assume that  $\phi_A \gg \phi_B$ , and then set  $\chi_{\pm} \approx w$  in Eqs. (22a) and (22b) to derive a single differential equation for  $w$ . The resulting equation is similar to Eq. (19) with  $Q_{\pm}(r) = q_{\pm}(r) \pm [E - V_{\text{QD}}(r)]t_c/\gamma^2$  when  $V_b = 0$ . This approximate equation is particularly good for small values of  $m$  and  $V_W$ . As an example, at  $V_W = 31$  meV the relative error is about 0.5% for  $m = -4$  but this quickly increases to 5% for  $m = -16$ .

The results in Fig. 2 and Fig. 3 are for  $s = 2$  and we have confirmed that good agreement between exact and approximate energies is found for different values of  $s$  (Appendix A). We briefly explore the role of  $s$  in Fig. 4, where we plot the

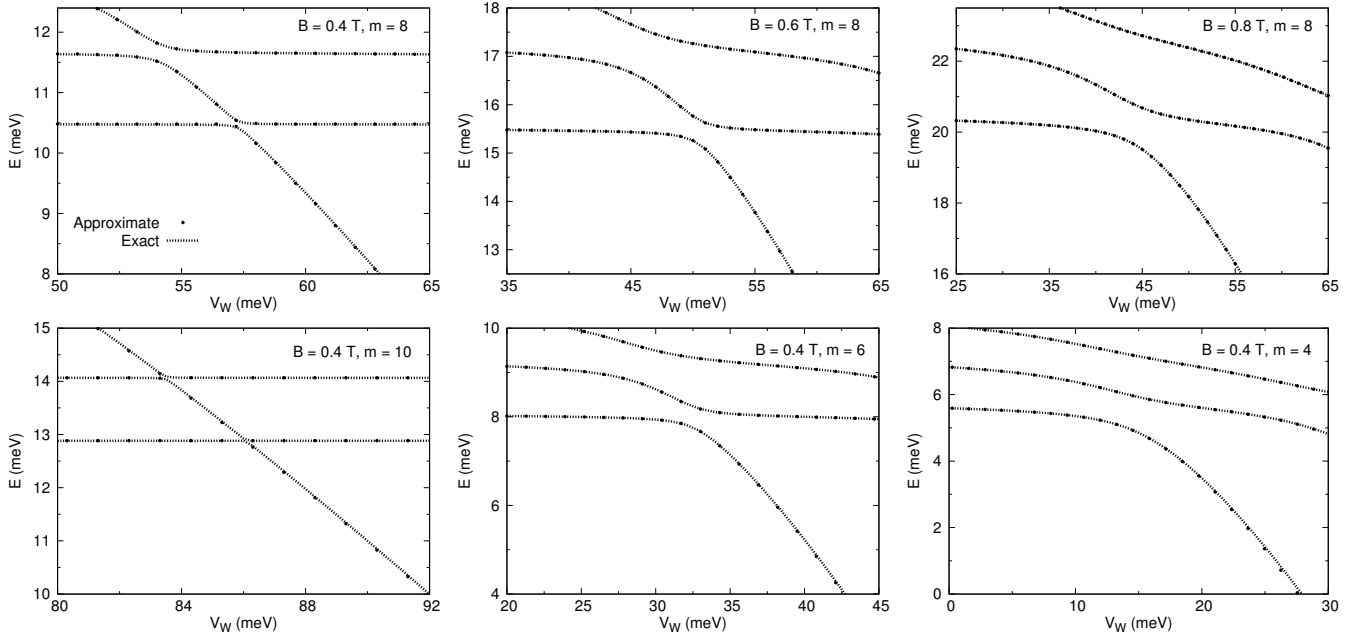


FIG. 5. Exact and approximate QD energy levels as a function of QD potential well at different magnetic fields  $B$  and angular momenta  $m$  for  $s = 2$  and  $V_b = 0$ . Approximate QD levels are derived from the numerical solution of Eq. (19).

QD levels as a function of the potential well width  $L_W$ . Here, the potential well is fixed and equal to  $V_W \approx E_L$ , so for this reason the QD energy tends to  $E \approx 0$  with  $L_W$ . This behaviour is robust and agrees with the approximate Eq. (27). This confirms the fact that the decrease of a QD level from the bulk Landau level cannot be greater than  $V_W$ , and according to Fig. 4 for larger  $s$  values the QD energy saturates at smaller potential widths.

We now proceed to demonstrate another interesting regime which can be approximately studied and seems to be mostly unexplored by earlier exact numerical studies of QDs in BLG. This regime can be more easily identified at low magnetic fields and potential widths. The key requirement is the potential well region to be different from the region where the original Landau state is localised. A narrow potential well tends to confine the states near the centre,  $r \approx 0$ , whereas a small magnetic field away from the centre. Tuning  $V_W$  can give rise to anticrossing points for energies  $E > V_{\text{asym}}$ , and the function  $Q_+$  has two positive maxima as illustrated in Fig. 1(d). To obtain the approximate QD levels in this regime we perform a numerical solution of Eq. (19) and present various examples in Fig. 5. We focus on the few lowest anticrossing points and choose the magnetic field to be relatively low,  $B < 1$  T, so that the Landau states to be localised away from the centre. The results in Fig. 5 indicate that both  $B$  and  $m$  should have suitable values in order to resolve the anticrossings.

In Fig. 5 the energy level that arises from the potential well shifts downwards with  $V_W$ , in contrast the Landau level depends weakly on  $V_W$ . As the  $B$  field decreases the Landau state shifts away from the centre, therefore, its overlap with the state localised in the potential well weakens. Consequently, the anticrossing gap starts to close as seen in Fig. 5 at  $B = 0.4$  T and  $m = 8$ . The opposite situation occurs for

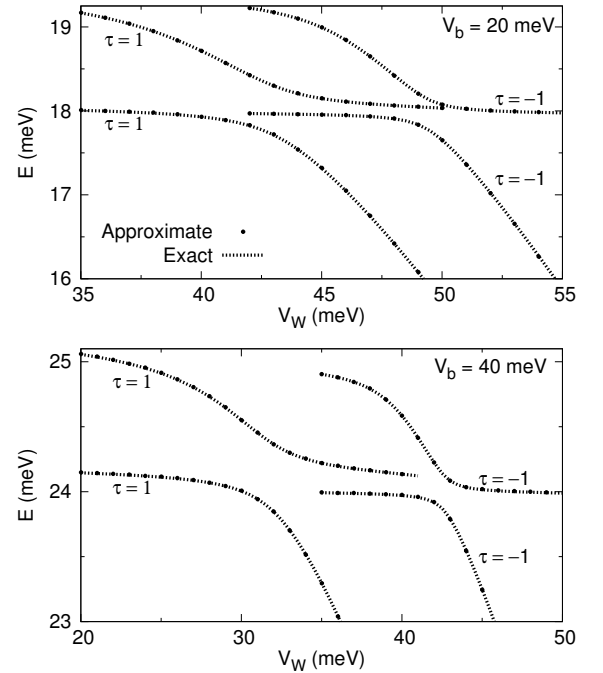


FIG. 6. Exact and approximate QD energy levels as a function of QD potential well in biased BLG for  $\tau = \pm 1$ ,  $B = 0.6$  T,  $m = 8$ ,  $L_W = 40$  nm, and  $s = 2$ . Approximate QD levels are derived from the numerical solution of Eq. (19).

smaller  $m$  values for which the Landau state strongly overlaps with the potential well state leading to a gap opening; see for example Fig. 5 at  $B = 0.4$  T and  $m = 4$ . The fact that the anticrossing is formed for  $E > V_{\text{asym}}$ , thus  $E - V_{1,2} \neq 0$ ,

suggests that to a good approximation the QD energy levels can be obtained from a simplified function  $Q_+$ . We have confirmed that by neglecting all the terms containing derivatives of  $V_{1,2}$  in  $Q_+$  [Eq. (20)] reproduces the exact energy characteristics.

Finally, in Fig. 6 we illustrate the formation of an anticrossing point in biased BLG for the two valleys. As in the zero-bias case, the approximate QD levels agree very well with the exact levels and we have confirmed that similar agreement is achieved at different magnetic fields and QD parameters beyond the anticrossing point regime. In biased BLG the function  $Q_+$  defined in Eq. (20) can acquire an imaginary part since the square-root can be negative when  $\kappa < 0$ . Provided that this imaginary part arises far away from the region where  $Q_+$  is solely real, with  $Q_+ > 0$ , the approximate energies can be obtained in the same way as for  $V_b = 0$ . The present work focuses on this regime only, hence, we can numerically solve the approximate Eq. (19) or use directly Eq. (25) to extract the approximate energies.

The accuracy of the harmonic oscillator formula, Eq. (25), depends on how well the parabolic term can approximate  $Q_+$  in Eq. (24). This, however, cannot be predicted in advance (Appendix A) due to the many terms involved in the approximate equations, as well as the broad range of the various physical parameters. Our numerical investigation suggests that the approximate results are usually less accurate for negative angular momenta and, in general, for smaller absolute values of angular momenta. For small energies, especially near zero, the relative errors can be large but the correct characteristics can still be predicted. In contrast, the relative errors tend to be smaller at higher magnetic fields and larger QD energies as well as for larger values of  $L_W$ . Additionally, the accuracy of the approximate QD levels derived from Eq. (25) can be improved by numerically solving the approximate Eq. (19).

## VI. CONCLUSION

We considered a QD in bilayer graphene defined by a realistic continuous potential well in a constant magnetic field. We started with the four-component continuum model and demonstrated some regimes where the QD energy levels can be obtained from simplified approximate equations. The basic advantage is that the approximate equations involve a single-component wavefunction and thus provide pedagogical insight into the physics of QDs. The approximate equations are applicable to a general form of the QD potential with either a soft-wall or hard-wall quantum well. The equations clarify in a transparent way how the quantum dot confinement changes by increasing the strength of the quantum well and the magnetic field, as well as how the QD levels emerge from the bulk Landau levels.

We proved the efficacy of the approximate method by comparing the approximate energies with the exact energies derived from the four-component continuum model in BLG. We found that the approximate energy levels as a function of the magnetic field and QD potential well exhibit the correct general features, such as for example, anticrossing points as well

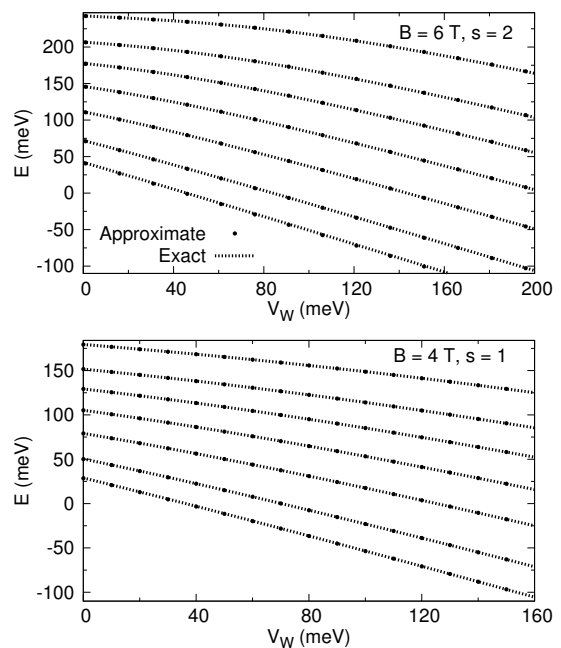


FIG. 7. As in Fig. 2 for  $L_W = 40$  nm and different  $B$  and  $s$ .

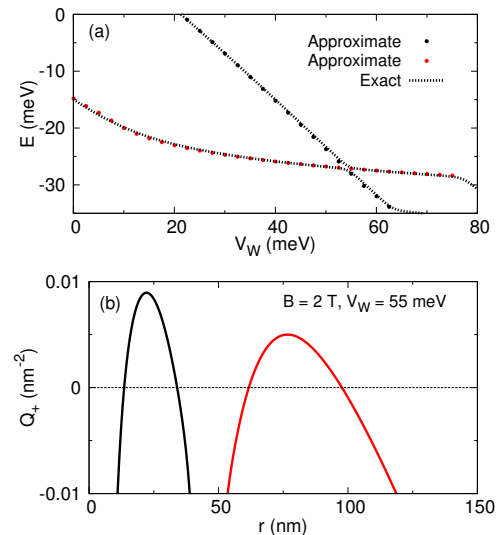


FIG. 8. (a) Exact and approximate QD energy levels as a function of QD potential well for  $B = 2$  T,  $s = 2$ ,  $m = 2$ . Approximate QD levels are derived from Eq. (25) for  $n = 0$ . (b) Near the anticrossing point  $Q_+$  has two maxima: approximate energies shown in black (red) are derived from left (right) maximum.

as a linear dependence on the dot potential, and agree very well with the exact energy levels in a broad range of QD parameters. We demonstrated various realistic regimes where the relative error can be vanishingly small. Semiclassical and quantum super-symmetric methods might be interesting alternative frameworks to approximately explore QD physics in bilayer graphene.

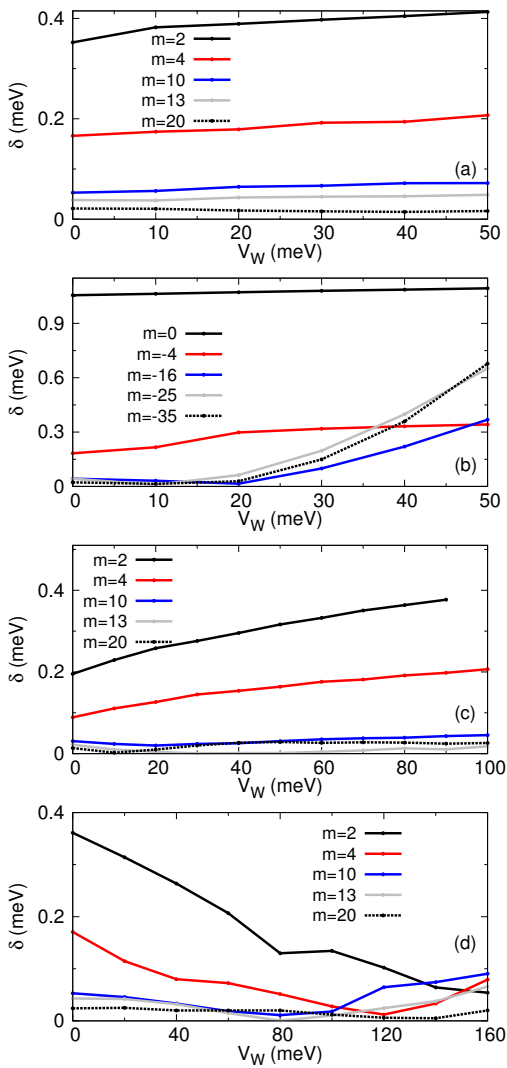


FIG. 9. Absolute difference between exact and approximate QD energy levels as a function of QD potential well for different angular momenta. Approximate QD levels are derived from Eq. (25) for  $m \neq 0$  and from Eq. (19) for  $m = 0$ . (a)  $B = 4$  T,  $L_W = 100$  nm,  $s = 2$ , (b)  $B = 4$  T,  $L_W = 100$  nm,  $s = 2$ , (c)  $B = 2$  T,  $L_W = 100$  nm,  $s = 2$ , and (d)  $B = 4$  T,  $L_W = 40$  nm,  $s = 1$ .

### Appendix A: Additional examples of quantum dot energies

We continue in this appendix the investigation of the QDs for a few more cases. Exact and approximate QD energies for

different parameters are shown in Fig. 7. Similar to the results examined in the main text (see Fig. 2) the approximate energies exhibit the correct behaviour and are in a good agreement with the exact energies. By increasing  $B$  the QD energies are brought closer to the linear regime described by the approximate Eq. (27), while a smaller  $s$  affects mostly the lowest QD energies.

Figure 8(a) presents a typical example where two QD energies form an anticrossing point for energies  $E < V_{\text{asym}}$ . Here, the two QD energies emerge from a positive and a negative Landau level respectively. As described in Sec. IV, the approximate method can capture the correct dependence on the potential well  $V_W$  but the anticrossing point cannot be resolved. Instead the approximate method predicts a crossing point. Depending on the QD energy and the value of  $V_W$  the function  $Q_+$  [Eq. (20)] has one or two positive maxima. Near the anticrossing point  $Q_+$  has two maxima separated by a region where a singular point dominates [Fig. 8(b)]. The two approximate QD energies in Fig. 8(a) are computed by focusing on each maximum separately, finding the corresponding point  $r_0$ , and finally solving Eq. (25) for  $n = 0$ .

Finally, in Fig. 9 we quantify the absolute difference,  $\delta$ , between the exact and approximate energies for a few characteristic examples. As detailed in the main text  $\delta$  remains small enough enabling the approximate method to capture all the basic characteristics of the exact QD levels derived from the four-component model. In Fig. 9 the range of  $V_W$  ensures that no anticrossing points are formed for  $E < V_{\text{asym}}$ . The dependence of  $\delta$  on  $V_W$  is sensitive to the exact QD parameters and cannot be rigorously predicted, however, we have confirmed that the same overall behaviour as in Fig. 9 is found for different parameters. The worst approximation corresponds to  $m = 0$  since the function  $Q_+$  has no positive maximum, see Sec. IV and Fig. 1(a). For this reason the approximate Eq. (25) cannot be applied and for  $m = 0$  we need to use Eq. (19). In this case the relative error drops below 5% only when  $V_W \gtrsim 35$  meV. In contrast, in order to derive the approximate energies for  $m \neq 0$  in Fig. 9 we use the harmonic oscillator formula, Eq. (25), which offers a more pedagogical insight. The more accurate Eq. (19) may also be used leading to a smaller  $\delta$ ; for example, in Fig. 9(b) the absolute difference can be reduced by one order of magnitude, namely,  $\delta \lesssim 0.07$  meV. This is a general conclusion. In particular, if the focus is on a rigorous investigation of the relative errors then Eq. (19) is more appropriate especially for small QD energies near zero.

[1] A. V. Rozhkov, A. O. Sboychakov, A. L. Rakhmanov, and F. Nori, Electronic properties of graphene-based bilayer systems, *Phys. Rep.* **648**, 1 (2016).  
 [2] E. McCann and M. Koshino, The electronic properties of bilayer graphene, *Rep. Prog. Phys.* **76**, 056503 (2013).  
 [3] L. M. Gachter, R. Garreis, J. D. Gerber, M. J. Ruckriegel, C. Tong, B. Kratochwil, F. K. de Vries, A. Kurzmann, K. Watanabe, T. Taniguchi, T. Ihn, K. Ensslin, and W. W. Huang, Single-

shot spin readout in graphene quantum dots, *PRX Quantum* **3**, 020343 (2022).  
 [4] A. L. Rakhmanov, A. V. Rozhkov, and A. O. Sboychakov, Magic radius of an AA-stacked bilayer graphene quantum dot, *Phys. Rev. B* **105**, 235415 (2022).  
 [5] D. R. da Costa, M. Zarenia, A. Chaves, G. A. Farias, and F. M. Peeters, Energy levels of bilayer graphene quantum dots, *Phys. Rev. B* **92**, 115437 (2015).

- [6] J. Velasco Jr, J. Lee, D. Wong, S. Kahn, H.-Z. Tsai, J. Costello, T. Umeda, T. Taniguchi, K. Watanabe, A. Zettl, F. Wang, and M. F. Crommie, Visualization and control of single-electron charging in bilayer graphene quantum dots, *Nano Lett.* **18**, 5104 (2018).
- [7] R. Garreis, C. Tong, J. Terle, M. J. Ruckriegel, J. D. Gerber, L. M. Gachter, K. Watanabe, T. Taniguchi, T. Ihn, K. Ensslin, and W. W. Huang, Long-lived valley states in bilayer graphene quantum dots, *Nature Physics* **20**, 428 (2024).
- [8] P. Recher, J. Nilsson, G. Burkard, and B. Trauzettel, Bound states and magnetic field induced valley splitting in gate-tunable graphene quantum dots, *Phys. Rev. B* **79**, 085407 (2009).
- [9] J. Bucko, F. Schafer, F. Herman, R. Garreis, C. Tong, A. Kurzmann, T. Ihn, and E. Greplova, Automated reconstruction of bound states in bilayer graphene quantum dots, *Phys. Rev. Applied* **19**, 024015 (2023).
- [10] D. R. da Costa, M. Zarenia, A. Chaves, G. A. Farias, and F. M. Peeters, Analytical study of the energy levels in bilayer graphene quantum dots, *Carbon* **78**, 392 (2014).
- [11] J. M. Pereira, P. Vasilopoulos, and F. M. Peeters, Tunable quantum dots in bilayer graphene, *Nano Lett.* **7**, 946 (2007).
- [12] S. Moller, L. Banszerus, A. Knothe, C. Steiner, E. Icking, S. Trellenkamp, F. Lentz, K. Watanabe, T. Taniguchi, L. I. Glazman, V. I. Fal'ko, C. Volk, and C. Stampfer, Probing two-electron multiplets in bilayer graphene quantum dots, *Phys. Rev. Lett.* **127**, 256802 (2021).
- [13] M. Mirzakhani, F. M. Peeters, and M. Zarenia, Circular quantum dots in twisted bilayer graphene, *Phys. Rev. B* **101**, 075413 (2020).
- [14] M. Eich, F. Herman, R. Pisoni, H. Overweg, A. Kurzmann, Y. Lee, P. Rickhaus, K. Watanabe, T. Taniguchi, M. Sigrist, T. Ihn, and K. Ensslin, Spin and valley states in gate-defined bilayer graphene quantum dots, *Phys. Rev. X* **8**, 031023 (2018).
- [15] A. Kurzmann, M. Eich, H. Overweg, M. Mangold, F. Herman, P. Rickhaus, R. Pisoni, Y. Lee, R. Garreis, C. Tong, K. Watanabe, T. Taniguchi, K. Ensslin, and T. Ihn, Excited states in bilayer graphene quantum dots, *Phys. Rev. Lett.* **123**, 026803 (2019).
- [16] K. Hecker, L. Banszerus, A. Schapers, S. Moller, A. Peters, E. Icking, K. Watanabe, T. Taniguchi, C. Volk, and C. Stampfer, Coherent charge oscillations in a bilayer graphene double quantum dot, *Nature Communications* **14**, 7911 (2023).
- [17] G. Giavaras, P. A. Maksym, and M. Roy, Electron confinement in single layer graphene quantum dots: Semiclassical approach, *Physica E* **42**, 715 (2010).
- [18] G. Giavaras, Energy spectra of graphene quantum dots induced between Landau levels, *Phys. Rev. B* **104**, 045430 (2021).
- [19] J. M. Pereira, F. M. Peeters, and P. Vasilopoulos, Landau levels and oscillator strength in a biased bilayer of graphene, *Phys. Rev. B* **76**, 115419 (2007).
- [20] G. Giavaras and F. Nori, Tunable quantum dots in monolayer graphene, *Phys. Rev. B* **85**, 165446 (2012).
- [21] G. Giavaras, Investigation of an energy dependent node creation in graphene quantum states, *Physica E* **144**, 115382 (2022).
- [22] L. I. Schiff, *Quantum Mechanics* (McGraw-Hill, New York, 1968).
- [23] G. Giavaras, P. A. Maksym, and M. Roy, Magnetic field induced confinement-deconfinement transition in graphene quantum dots, *J. Phys.: Condens. Matter.* **21**, 102201 (2009).